Iranian Journal of Science and Technology, Transactions of Mechanical Engineering (2024) 48:103–118
https://doi.org/10.1007/s40997-023-00646-w

RESEARCH PAPER

Numerical Simulation of Pitching Airfoil in the Slip Flow Regime

Y. Amini[1]

Received: 26 August 2021 / Accepted: 15 March 2023 / Published online: 12 April 2023

Abstract

In this paper, a pitching NACA 0012 airfoil is simulated in the slip flow regime by solving the Navier–Stokes equations subjected to the Maxwell slip and Smoluchowski jump boundary conditions. The rhoCentralDyMFoam solver of the OpenFOAM software has been modified to handle these boundary conditions. The effects of several parameters such as reduced frequency, mean angle of attack, amplitude of oscillation and the Knudsen (Kn) number on aerodynamic coefficients are investigated. It was shown that Kn has no significant effect on lift coefficient but changes drag coefficient significantly. Moreover, the reduced frequency changes the lift coefficient considerably but its effect on the drag coefficient is negligible.

Keywords Maxwell slip · Pitching airfoil · Slip flow regime · Smoluchowski jump · OpenFOAM · NACA 0012

1 Introduction

In the recent years, many researchers have studied rarefied gas flows such as flows in micro- or nano-devices and fluid flows near hypersonic aircraft at high elevation. The rarefied gas flow is defined as flow that has a large value of Knudsen number (Kn). This number is described as the molecular mean free path (λ) divided by the characteristic length of the flow (L). Fluid flows can be categorized by the Knudsen number into four different regimes (Chambré and Schaaf 1961; Zhang et al. 2012). The first is the continuum regime with Kn of smaller than 0.001. In this regime, the Navier–Stokes (N–S) equations with the no-slip boundary condition are the governing equations. The second is the slip regime with Kn between 0.001 and 0.1. Similar to the continuum regime, in the slip regime, governing equations of flow are the N–S equations. However, the slip-velocity and temperature-jump boundary conditions should be used instead of no-slip boundary conditions (Gad-el-Hak 1999; Ho and Tai 1998). The third flow regime is the transition flow with $0.1 < \mathrm{Kn} < 10$, and the last flow regime is the free molecular flow with $\mathrm{Kn} > 10$. In the transition and free molecular regimes, the N–S equations are not valid and other numerical methods such as the direct simulation Monte Carlo (DSMC) (Bird 1976) or Boltzmann equation (Lilley and Sader 2008) should be used for simulating fluid flows.

Amini et al. (2012) simulated different types of nose cone shapes in the rarefied gas condition by using the DSMC method. They considered fluid flows as a mixture of gases. In another work, Amini et al. (2018) investigated the aerodynamics of the NACA 0012 airfoil with connected Gurney flap in the rarefied gas condition and Mach number of 2. They studied the effects of different parameters such as the Knudsen numbers, Gurney flap height and angles of attack. Fan et al. (2001) simulated gas flows around the NACA 0012 airfoil in the rarefied gas condition at different Mach numbers by using both the N–S equations with slip/jump boundary conditions and the DSMC method. In order to remove statistical fluctuations of DSMC results in subsonic flows, they used the information preservation type of the DSMC method. Shoja-Sani et al. (2014) calculated the lift and drag coefficients of the NACA 0012 airfoil at high Knudsen numbers by using both the N–S equations with slip/jump boundary conditions and the DSMC method. They utilized the dsmcFoam solver of the OpenFOAM package. They showed that by increasing the Knudsen number, the drag coefficient increases. Le et al. (2015) investigated the rarefied gas flows around NACA 0012 by solving the N–S equations subjected to the first and second orders of the slip and jump boundary conditions. They considered two different Mach numbers of 0.8 and 2. They have shown that in comparison with the first-order boundary conditions, the lift and drag coefficients calculated by second-order boundary conditions have better

---

✉ Y. Amini
Aminiyasser@pgu.ac.ir

[1] Department of Mechanical Engineering, Persian Gulf University, Bushehr 75169, Iran

agreement with the lift and drag coefficients obtained by the DSMC method. Allegre et al. (1986, 1987) studied the subsonic and supersonic flows around the NACA 0012 airfoil at a Knudsen number of 0.026.

The dynamic stall denotes unsteady flow separation arising on airfoils during a pitching motion and have been investigated extensively in recent years (Favier et al. 1988; Ko and McCroskey 1997; Martin et al. 1974; Wang et al. 2010). When the airfoil rotates in the upward direction, a leading-edge vortex (LEV) is developed and moves along the upper surface of the airfoil. This vortex reduces pressure on the upper surface and causes the maximum lift coefficient to increase. At the onset of downward rotation of the airfoil, this vortex is quickly separated from the upper surface and leads to a great reduction in the lift. This phenomenon is called dynamic stall and produces a hysteresis loop of force and moment on the airfoil that can lead to a break in the wing. Therefore, occurrence of the dynamic stall limits the performance of wings, substantially. Wernert et al. (1996) and Leishman (1990) indicated that a second local maximum in the lift coefficient's curve is created due to generation of a second vortex in the down stroke phase of the airfoil rotation. Amiralaei et al. (2010) studied performance of the NACA0012 airfoil for a pitching motion in laminar flows, numerically. Effects of different factors such as frequency of motion, amplitude of motion and the Reynolds number on the lift and drag coefficients were studied. Wang et al. (2010) modeled the dynamic stall of a pitching NACA0012 airfoil at low Reynolds number and turbulent flow, numerically. Gharali and Johnson (2013) studied the effects of pulsating inlet velocity on the aerodynamic performance of the NACA0012 airfoil in a pitching motion and turbulent flow.

In this paper, unsteady flow around the NACA0012 airfoil during a pitching motion in a rarefied gas condition is simulated, numerically. The dynamic stall is occurred in a pitching motion and affects the lift and drag coefficients, significantly. The effects of Knudsen number, pitching amplitude, mean angle of attack and pitching frequency on the lift and drag coefficients are examined.

2 Governing Equations

In the slip regime, the N–S equations subjected to the slip/jump boundary conditions are valid. These equations for unsteady and compressible flow are written as follows:

Conservation of mass

$$\frac{\partial \rho}{\partial t} + \nabla \cdot [\rho \boldsymbol{V}] = 0 \tag{1}$$

Conservation of momentum

$$\frac{\partial (\rho \boldsymbol{V})}{\partial t} + \nabla \cdot [\rho \boldsymbol{V}\boldsymbol{V}] = -\nabla P + \nabla \cdot \boldsymbol{\tau} \tag{2}$$

where $\boldsymbol{V}$, ρ and τ are the velocity, the gas density and the shear stress tensor. For the Newtonian fluid τ is defined as:

$$\boldsymbol{\tau} = \mu\left[\nabla \boldsymbol{V} + (\nabla \boldsymbol{V})^{\mathrm{T}}\right] \tag{3}$$

where μ is the dynamic viscosity

Conservation of total energy

$$\frac{\partial (\rho E)}{\partial t} + \nabla \cdot [\boldsymbol{V}(\rho E)] + \nabla \cdot (\boldsymbol{V}P) + \nabla \cdot (\boldsymbol{\tau} \cdot \boldsymbol{V}) + \nabla \cdot \boldsymbol{q} = 0 \tag{4}$$

$$E = c_{\mathrm{V}} T + 0.5|\boldsymbol{V}|^2 \tag{5}$$

where E, c_{V} and T are the total energy, constant volume specific heat and temperature, respectively. q is the heat flux and it is evaluated by $q = -k_f \nabla T$. Here k_f represents the thermal conductivity. In the current study, perfect gas behavior is assumed. Therefore, the following relation is considered in all simulations

$$P = \rho R T \tag{6}$$

where R is the specific gas constant.

2.1 The Velocity Slip and Temperature Jump Condition

For simulating the slip regime by using the N–S equations, imperfect momentum and energy accommodation over the surface should be modeled in the boundary conditions. These boundary conditions are the Maxwell slip and the Smoluchowski jump and are defined as follows (Karniadakis et al. 2006):

$$\boldsymbol{V} - \boldsymbol{V}_{\mathrm{w}} = -\frac{2-\sigma_{\mathrm{u}}}{\sigma_{\mathrm{u}}} \lambda \nabla_{\boldsymbol{n}}(\boldsymbol{S} \cdot \boldsymbol{V}) - \frac{2-\sigma_{\mathrm{u}}}{\sigma_{\mathrm{u}}} \frac{\lambda}{\mu} \boldsymbol{S} \cdot (\boldsymbol{n} \cdot \Pi) - \frac{3}{4} \frac{\mu}{\rho} \frac{\boldsymbol{S} \cdot \nabla T}{T} \tag{7}$$

$$T - T_{\mathrm{w}} = -\frac{2-\sigma_{\mathrm{T}}}{\sigma_{\mathrm{T}}} \frac{2\gamma}{(\gamma+1)Pr} \lambda \nabla_{n} T \tag{8}$$

where $\mathbf{n}$, σ_{u} and σ_{T} represent the unit normal vector of the surface, the tangential momentum accommodation factor and thermal accommodation factor, respectively. The subscript w refers to the wall properties and the tensor $\mathbf{S}$ is defined as $\mathbf{S} = \mathbf{I} - \mathbf{nn}$, where $\mathbf{I}$ is an identity tensor and Π is defined as:

$$\Pi = \mu(\nabla \boldsymbol{V})^{\mathrm{T}} - \frac{2}{3} \boldsymbol{I}_{\mathrm{tr}}(\nabla \boldsymbol{V}) \tag{9}$$

where subscript tr signifies the trace of tensor. In the present study, both accommodation factors are considered equal to one.

3 Numerical Method

3.1 Discretization of the NS Equations

In this study, rhoCentralDyMFoam solver in the OpenFOAM package is used for solving the governing equations subjected to the slip/jump boundary conditions (Greenshields et al. 2010). This is an explicit and density-based solver for solving the compressible and Newtonian flows with dynamic mesh motion. In this paper, the Maxwell slip and Smoluchowski jump boundary conditions of OpenFOAM are modified to handle the dynamic mesh capability. In rhoCentralDyMFoam, the second-order semi-discrete, non-staggered schemes of Kurganov and Tadmor (2000) and Kurganov et al. (2001) are used to interpolate field values in cell centers and discretization of a general tensor variable (ψ) is defined as follow (Greenshields et al. 2010).

The convective terms of the N–S equations can be discretized as (Kurganov et al. 2001; Kurganov and Tadmor 2000):

$$\iiint_{\forall} \nabla \cdot [\boldsymbol{u}\psi] \mathrm{d}\forall = \sum_f \boldsymbol{S}_f \cdot \left(\boldsymbol{u}_f \psi_f\right) = \sum_f \phi_f \psi_f \tag{10}$$

$$\sum_f \phi_f \psi_f = \sum_f \left[\alpha \phi_f + \psi_{f_+} + (1-\alpha)\phi_{f\_}\psi_{f\_} + \omega_f\left(\psi_{f\_} - \psi_{f_+}\right)\right] \tag{11}$$

where $\boldsymbol{S}_f$ and ω_f are the face area vector and diffusive volumetric flux, respectively. $\phi_f = \boldsymbol{S}_f \cdot \boldsymbol{u}_f$ is the volumetric flux. $\sum_f$ represents a summation over all faces of the cell. In the Kurganov-Tadmor (KT) and Kurganov-Noelle-Petrova (KNP) methods, the interpolation is divided into two directions, namely the flow inlet to the cell faces (f_+) and flow outlet to the cell faces ($f\_$). In this equation, ψ_{f_+} and $\psi_{f\_}$ represents the flux calculations at the f_+ and $f\_$ directions, respectively. These fluxes are evaluated as:

$$\begin{aligned} \psi_{f_+} &= \max\left(c_{f_+}\left|S_f\right| + \phi_{f_+}, c_{f\_}\left|S_f\right| + \phi_{f\_}, 0\right) \\ \psi_{f\_} &= \max\left(c_{f_+}\left|S_f\right| - \phi_{f_+}, c_{f\_}\left|S_f\right| - \phi_{f\_}, 0\right) \end{aligned} \tag{12}$$

where ϕ_{f_+} and $\phi_{f\_}$ are interpolated using the first-order upwind interpolation schemes. α and c_f is the weighting coefficient and the sound speed at the cell faces, respectively.

The weighting coefficient is defined as

$$\alpha = \begin{cases} 0.5 & \text{for KT scheme} \\ \frac{\psi_{f_+}}{\psi_{f_+} + \psi_{f\_}} & \text{for KNP scheme} \end{cases} \tag{13}$$

The diffusive volumetric flux $\left(\omega_f\right)$ is calculated from

$$\omega_f = \begin{cases} \alpha \max\left(\psi_{f_+}, \psi_{f\_}\right) & \text{for KT scheme} \\ \alpha(1-\alpha)\max\left(\psi_{f_+}, \psi_{f\_}\right) & \text{for KNP scheme} \end{cases} \tag{14}$$

In Eqs. (2) and (4), the gradient terms are discretized as:

$$\iiint_{\forall} \nabla\psi \, \mathrm{d}\forall = \sum_f \left[\alpha S_f \psi_{f_+} + (1-\alpha) S_f \psi_{f\_}\right] \tag{15}$$

Moreover, the discretized form of the Laplacian terms is presented as:

$$\iiint_{v} N \times (\Gamma N\psi) \, \mathrm{d}\forall = \iint_S \mathrm{d}S \cdot (\Gamma \nabla\psi) \approx \sum_f \Gamma_f S_f \cdot (\nabla\psi)_f \tag{16}$$

In the above equation, Γ stands for the diffusion coefficient and it is interpolated by averaging its values at adjacent cell centers.

3.1.1 Time Integration of the NS Equations

Since rhoCentralFoam is an explicit solver, solutions at the present time step are calculated from the obtained values of previous time step. In this explicit solver, to improve the time step limitation, a sequential approach is used to consider the diffusive terms as suitable implicit corrections. This solution algorithm includes three main steps (Greenshields et al. 2010):

Step 1 Solving the inviscid equations as follows:

$$\begin{aligned} &\left(\frac{\partial\left(\rho V'\right)}{\partial t}\right)_{\text{inv}} + \nabla \cdot \left(V\left(\rho V'\right)\right) + \nabla P = 0 \\ &\left(\frac{\partial\left(\rho E'\right)}{\partial t}\right)_{\text{inv}} + \nabla \cdot \left(V\left(\rho E' + P\right)\right) + \nabla \cdot (\tau \cdot V) = 0 \end{aligned} \tag{17}$$

In the above equations the prime denotes variables which are calculated by inviscid assumptions.

Step 2 Updating values of V and T from the solutions of Eq. (17). In this step, the temperature can be calculated by:

$$T = \frac{1}{C_V}\left[\frac{\rho\left(\rho E'\right)}{\rho} - \frac{|V'|^2}{2}\right] \tag{18}$$

Step 3 Solving the implicit form of diffusion equations for the primitive variables.

In this step, the velocity and the temperature can be updated as below:

$$\begin{aligned}&\left(\frac{\partial(\rho V)}{\partial t}\right)_{\text{vis}} - \nabla\cdot(\mu\nabla V) - \nabla\cdot\left(\tau_{\exp}\right) = 0\\&\left(\frac{\partial\left(\rho C_V T\right)}{\partial t}\right)_{\text{vis}} - \left(k_f \nabla T\right) = 0\end{aligned} \tag{19}$$

4 Problem Description

In this paper, a pitching NACA 0012 airfoil in rarefied condition is investigated. Figure 1 shows the schematic of the computational domain. In this figure, C is the chord length and α presents the angle of attack (AOA). The pitching rotation of the airfoil is specified by the following sinusoidal angular motion:

$$\alpha = \alpha_{\mathrm{m}} + \alpha_{\mathrm{A}} \sin(\omega t) \tag{20}$$

where α_{m} is the mean AOA, α_{A} is the pitch amplitude and ω denotes oscillation frequency. The center of rotation is placed at 0.25C from the leading edge of the airfoil. The inlet boundary is assumed as the free stream condition and Mach number and temperature of air at this boundary are 2 and 161 K, respectively. The temperature on the airfoil surface is 290 K. At the upper, lower and outlet boundaries, zero gradient in normal direction is applied for velocity, pressure and temperature variables. Maxwell slip velocity and temperature jump boundary condition are applied to the surface of the airfoil. Additionally, reduced frequency (k) of the pitching airfoil is defined as:

$$k = \frac{\omega C}{2U_\infty} \tag{21}$$

5 Mesh Independence Study

In order to investigate the independence of results from the numerical grid, three different high-quality structured meshes are used. The total number of cells in coarse, medium and fine meshes are 46,000, 91,000 and 174,000, respectively. The lift and drag coefficients of the NACA 0012 airfoil at $M = 2$ and Kn = 0.026 obtained from these meshes are compared in Tables 1 and 2, respectively. As can be seen, in all angles of attack (α), the difference

Table 1 Comparison of drag coefficient obtained by the DSMC method and those obtained by different meshes

	Coarse mesh	Medium mesh	Fine mesh	DSMC (Amini et al. 2018)
$\alpha = 0°$	0.3988	0.4065	0.4103	0.4109
$\alpha = 10°$	0.4496	0.4636	0.4621	0.4609
$\alpha = 20°$	0.6019	0.6145	0.6167	0.6194

Fig. 1 Schematics of the computational domain and an oscillating airfoil under pitching motion

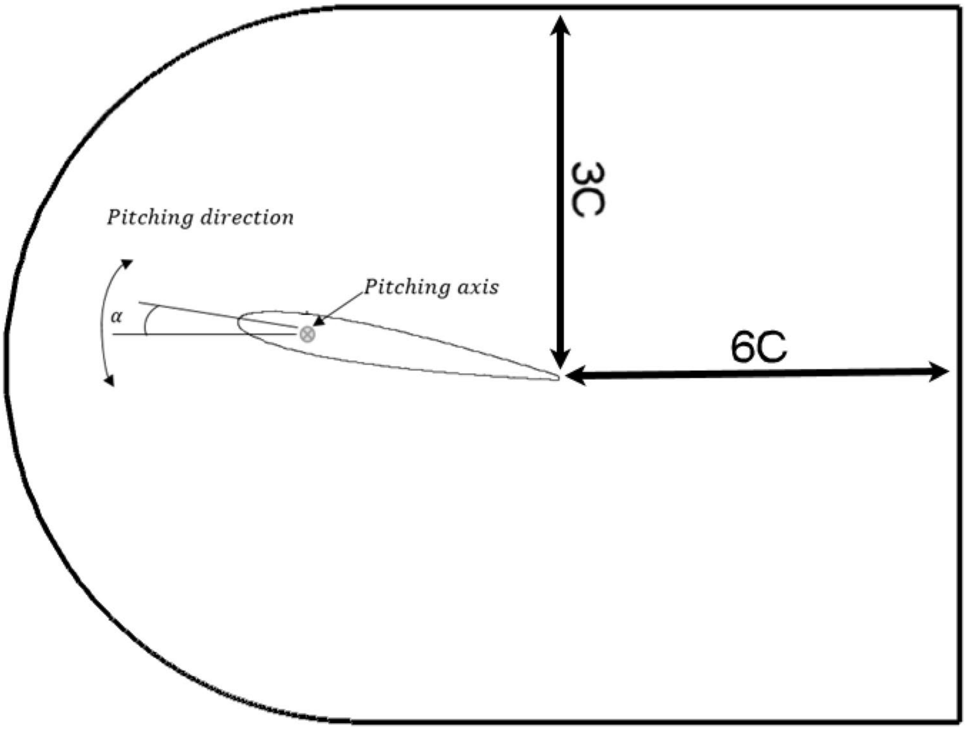

Table 2 Comparison of lift coefficient obtained by the DSMC method and those obtained by different meshes

	Coarse mesh	Medium mesh	Fine mesh	DSMC (Amini et al. 2018)
$\alpha = 5°$	0.1763	0.1844	0.1849	0.185
$\alpha = 10°$	0.3418	0.3529	0.3526	0.3523
$\alpha = 20°$	0.6518	0.6742	0.6749	0.6756

Table 3 Comparison between the present results of N–S equations with those given by Le et al. (2015) and Shoja-Sani et al. (2014)

AOA	Present results		Le et al. (2015) and Shoja-Sani et al. (2014)	
	C_D	C_L	C_D	C_L
0°	0.4065	–	0.3999	–
5°	0.41	0.1844	0.4107	0.1758
10°	0.4636	0.3529	0.4533	0.3511
15°	0.5214	0.5206	0.5223	0.5201
20°	0.6145	0.6742	0.6133	0.6757

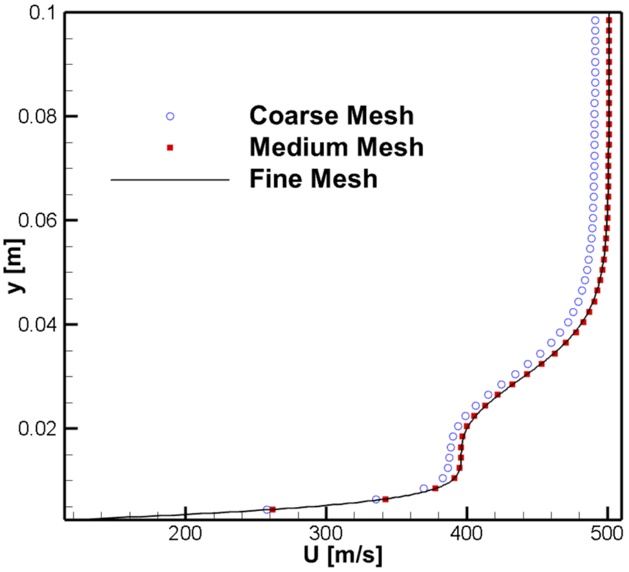

Fig. 3 Velocity profile on the upper surface of the airfoil for different meshes at Mach = 2, Kn = 0.026 and $x = 0.25$C

between values of lift and drag coefficients obtained by medium and fine meshes are very small. Therefore, in this study the medium mesh is used for simulation of a pitching NACA 0012 airfoil at $M = 2$.

In Fig. 2 the pressure coefficient and slip velocity distributions on the airfoil surface at Mach = 2, Kn = 0.026 and $\alpha = 20°$ for different meshes are presented. Also, the velocity profiles in the boundary layer for these meshes are presented in Fig. 3. As can be seem, these figures show that the results of medium mesh and fine mesh are adequately close to each other and consequently for reducing the CPU time, the medium mesh is used in the numerical simulations of this work.

The medium grid and its close-up views are shown in Fig. 4. Also, the number of nodes on airfoil surface in this mesh is 700 while the number of nodes on the airfoil surface in coarse and fine meshes are 500 and 1000, respectively.

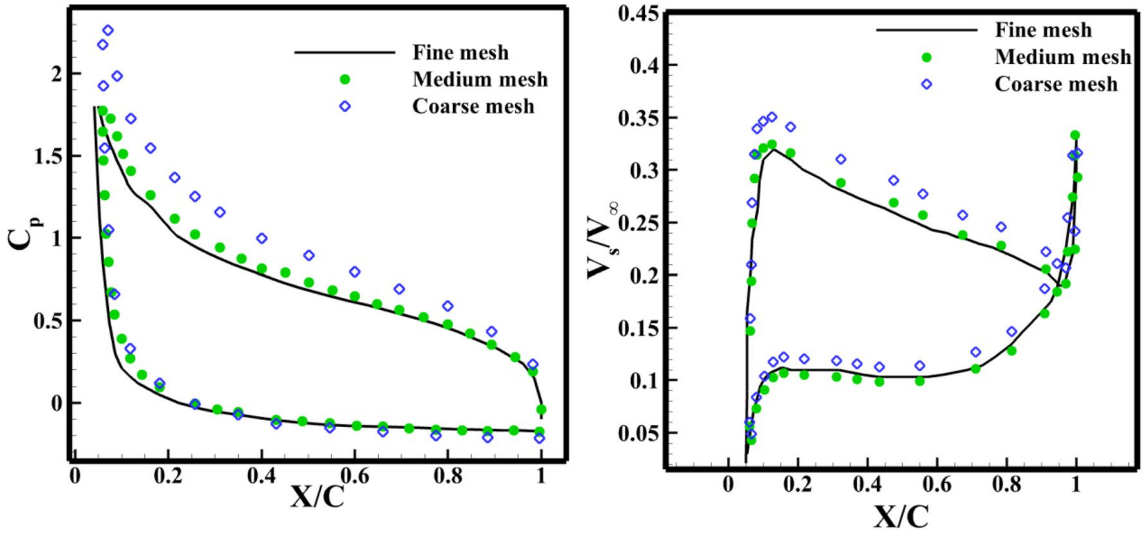

Fig. 2 Mesh independence study at Mach = 2, Kn = 0.026 and $\alpha = 20°$ **a** pressure coefficient, **b** slip velocity on airfoil

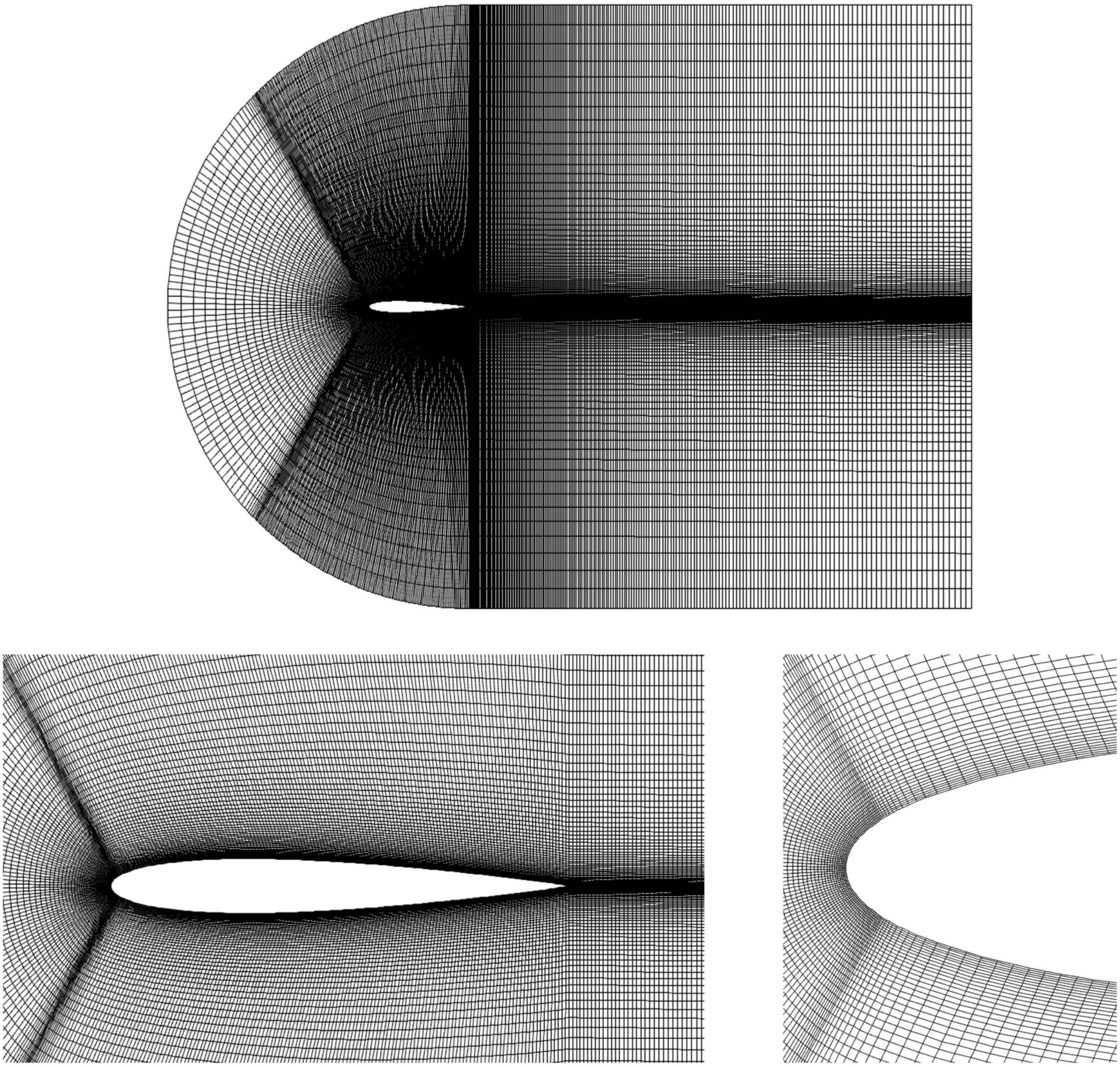

Fig. 4 Computational grid around the hydrofoil and its detail view

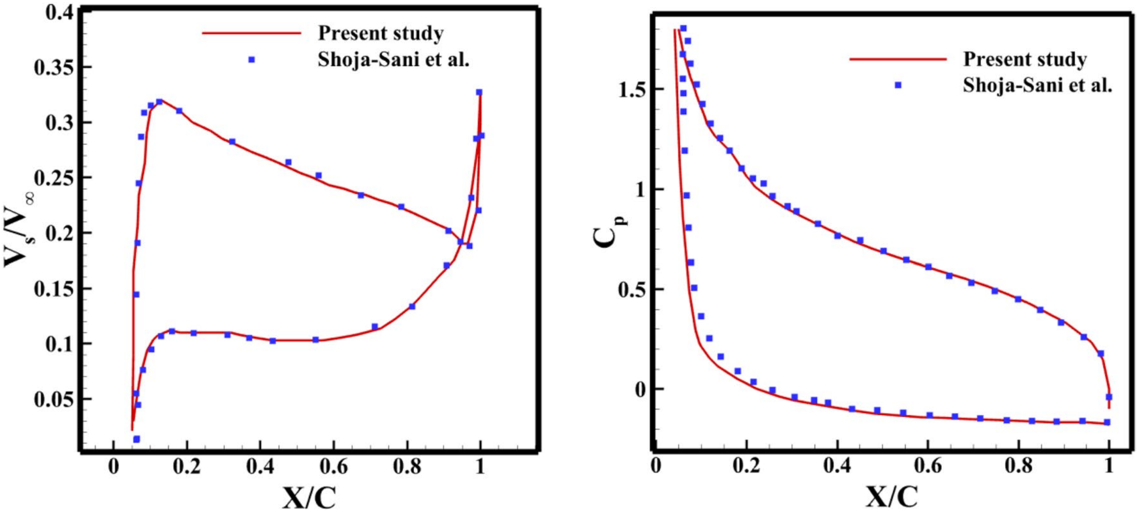

Fig. 5 Comparison of slip velocity and pressure coefficient on the surface of NACA 0012 airfoil at Kn = 0.026 and $M = 2$

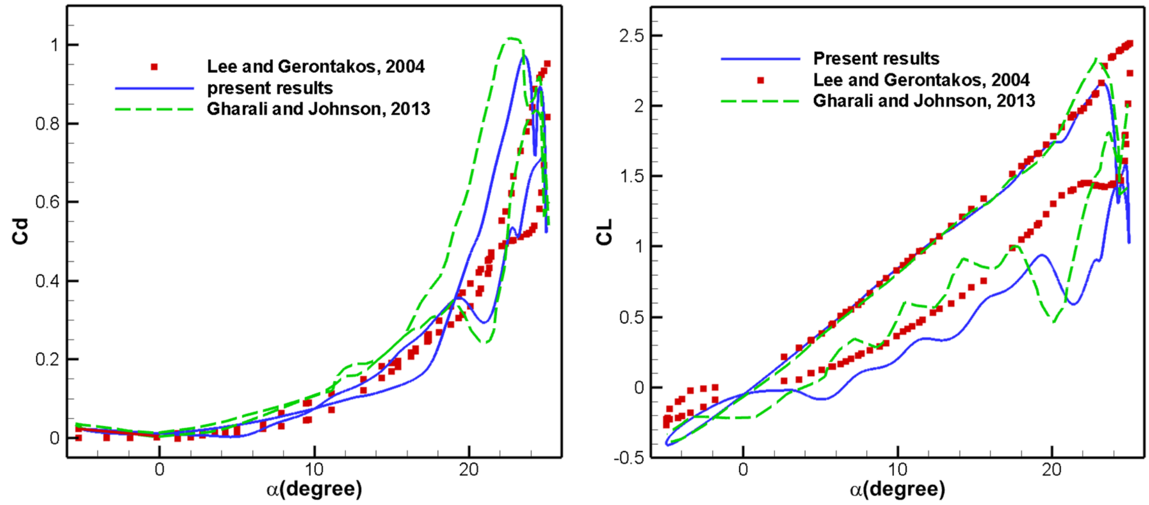

Fig. 6 Comparison of the present lift and drag coefficients with previous experiments and numerical results

Fig. 7 Comparison of the lift and the drag coefficients between the slip and no-slip boundary conditions at Kn = 0.001

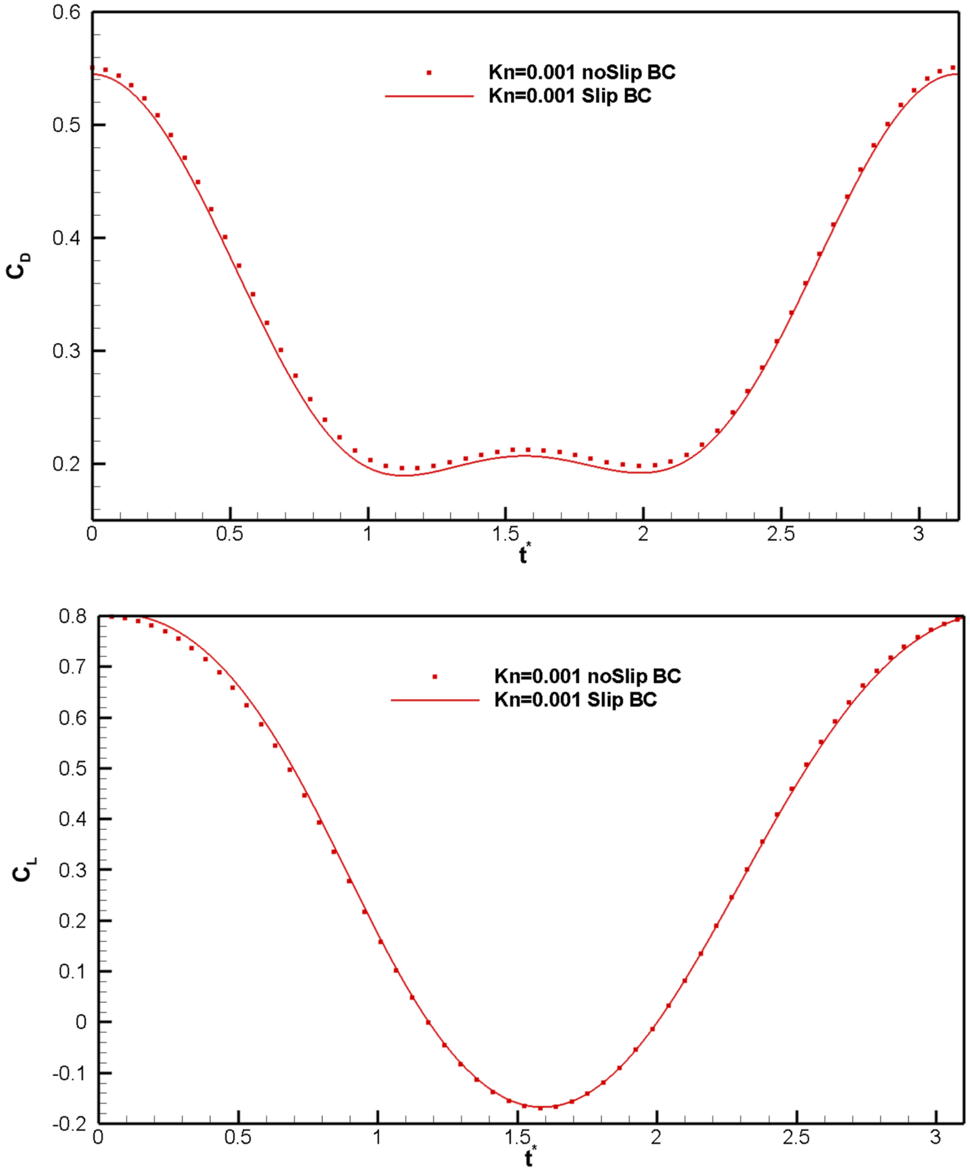

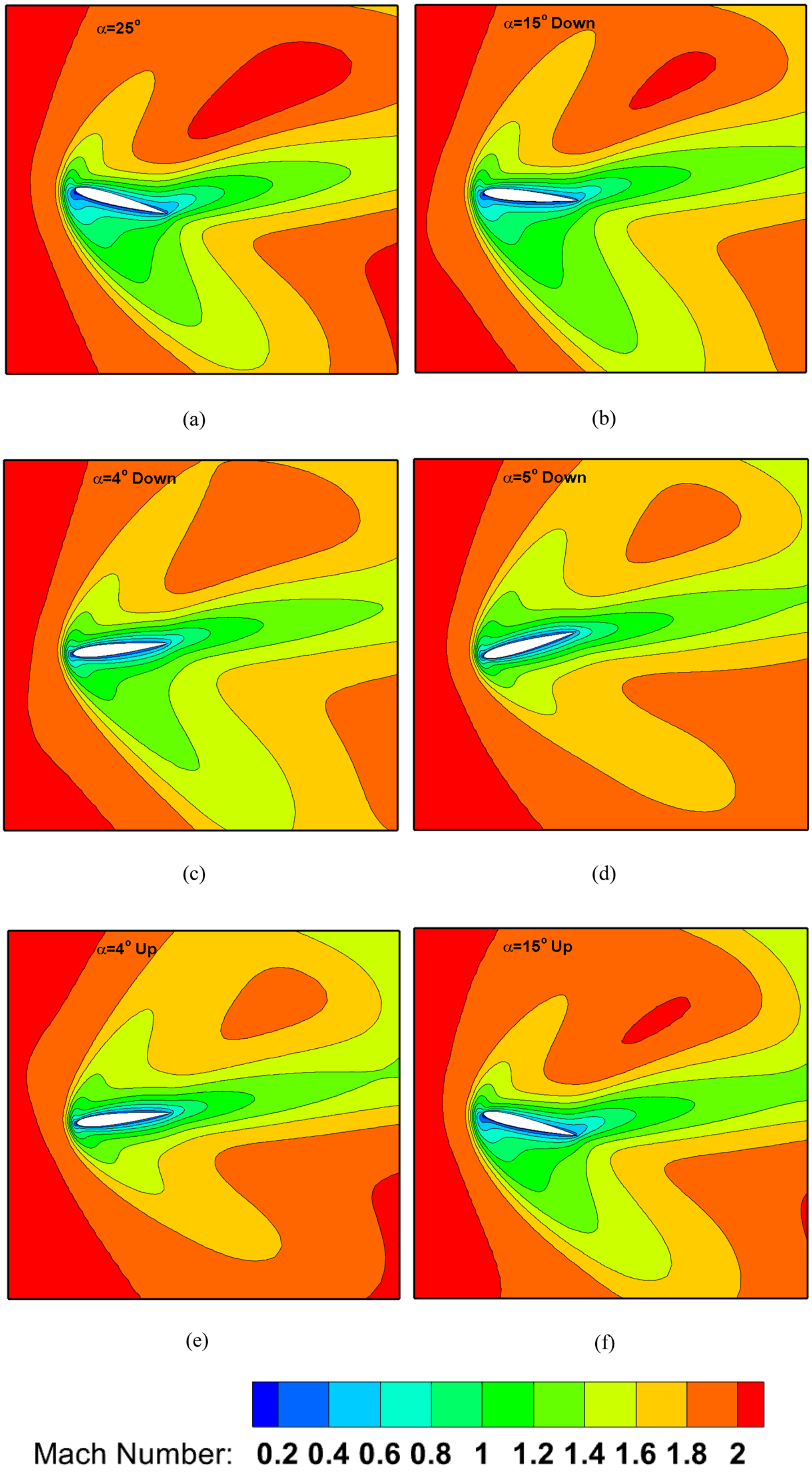

Fig. 8 Contour of Mach number at different angles of attack for Kn = 0.026, $k = 0.1$, $\alpha_{\mathrm{m}} = 10°$ and $\alpha_{\mathrm{A}} = 15°$

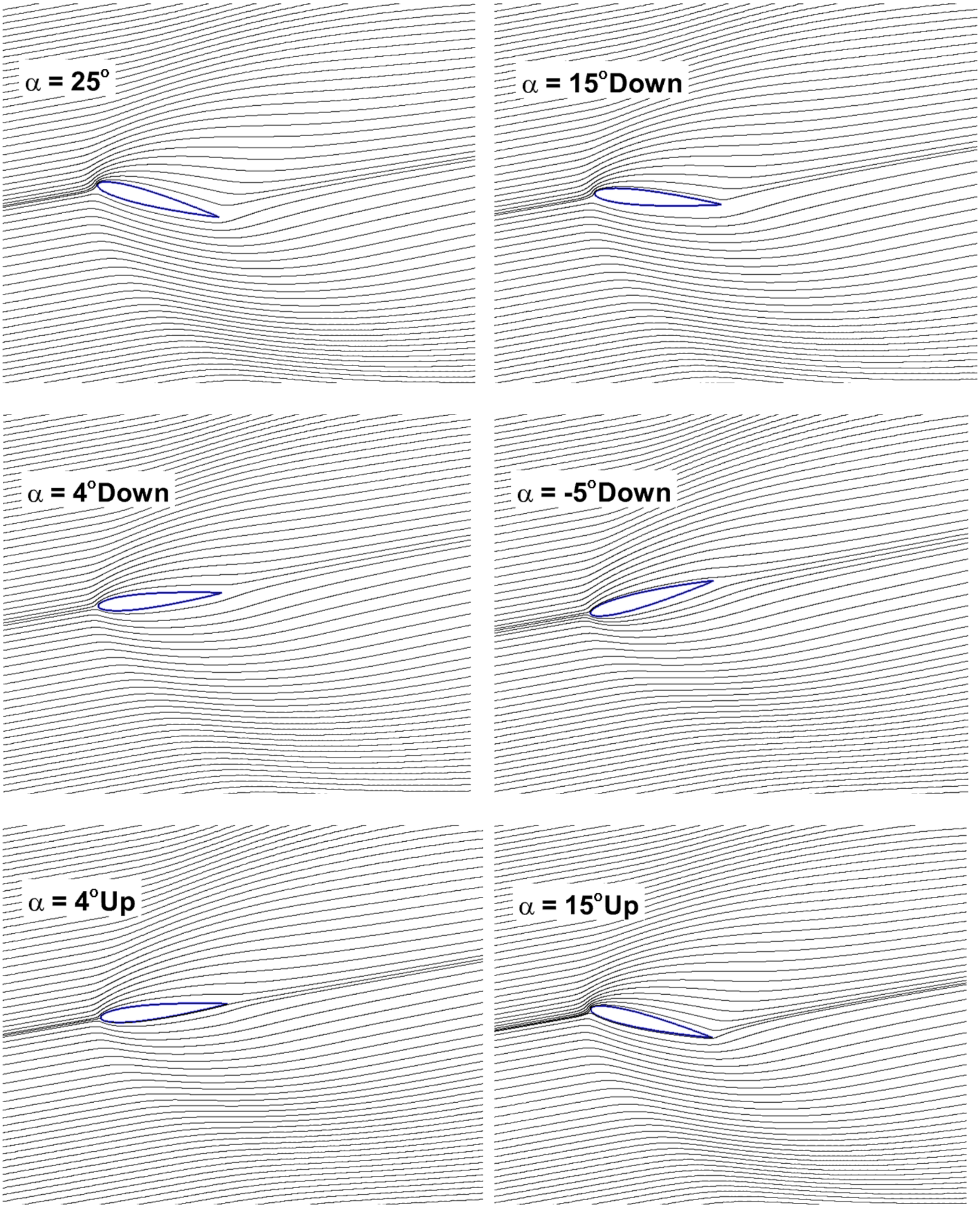

Fig. 9 Contour of temperature at different angles of attack for $\mathrm{Kn}=0.026$, $k=0.1$, $\alpha_{\mathrm{m}}=10°$ and $\alpha_{\mathrm{A}}=15°$

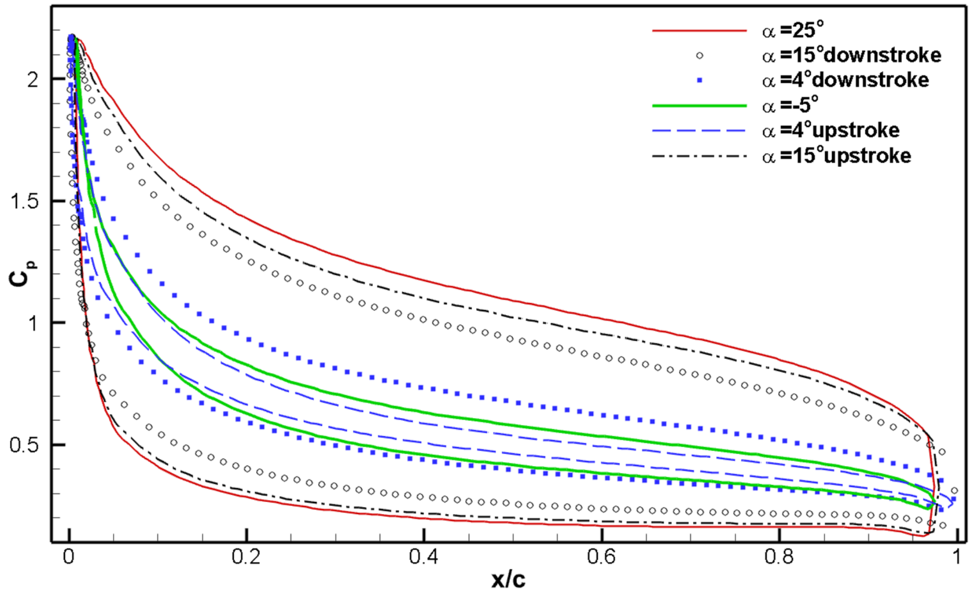

Fig. 10 The pressure coefficient distribution over the airfoil for Kn = 0.026, $k = 0.1$, $\alpha_m = 10°$ and $\alpha_A = 15°$

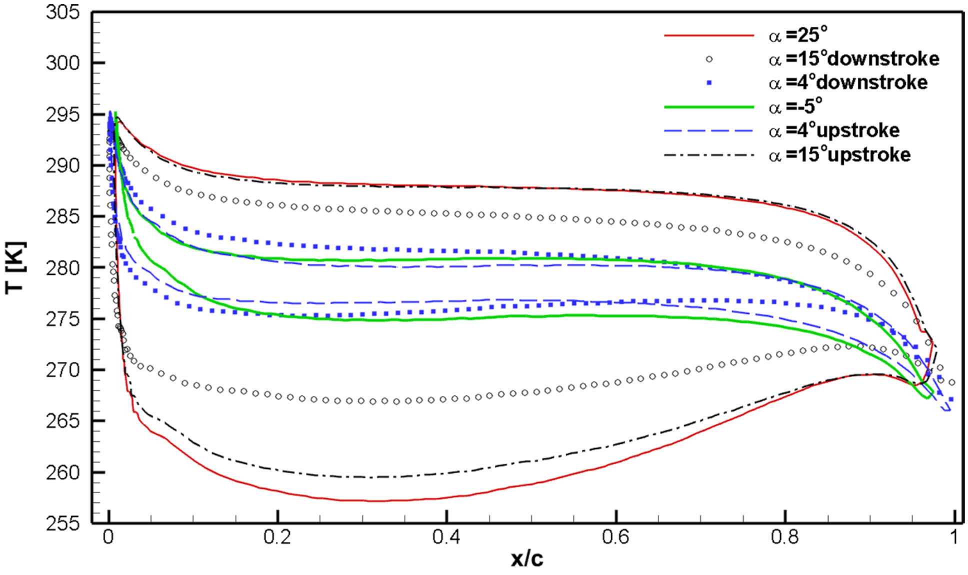

Fig. 11 The temperature distribution over the airfoil for Kn = 0.026, $k = 0.1$, $\alpha_m = 10°$ and $\alpha_A = 15°$

6 Validation

In Table 3, obtained values of lift and drag coefficients for NACA 0012 at Kn = 0.026, $M = 2$ and wide range of angles of attack are compared with those given by Le et al. (2015) and Shoja-Sani et al. (2014). As Table 3 indicates, maximum discrepancies between the current predictions for drag and lift coefficient and those reported by references is less than 4.9%.

In Fig. 5, the obtained values for slip velocity and pressure coefficient on the NACA 0012 airfoil surface at Kn = 0.026, $M = 2$ and AOA = 20° are compared with those of presented by Shoja-Sani et al. (2014). The discrepancy between the two results is sufficiently small, and they are in a good agreement.

In another test case, the aerodynamic coefficients of a pitching airfoil at the no-slip condition are compared with experimental (Lee and Gerontakos 2004) and numerical (Gharali and Johnson 2013) results. Here, at a reduced frequency of $k = 0.1$ the airfoil rotates so that the angle of attack changes by $\alpha = 10° + 15° \sin(18.67t)$. In Fig. 6 the present lift and drag coefficients are compared with experimental (Lee and Gerontakos 2004) and numerical (Gharali and Johnson 2013) results. At the up-stroke motion of

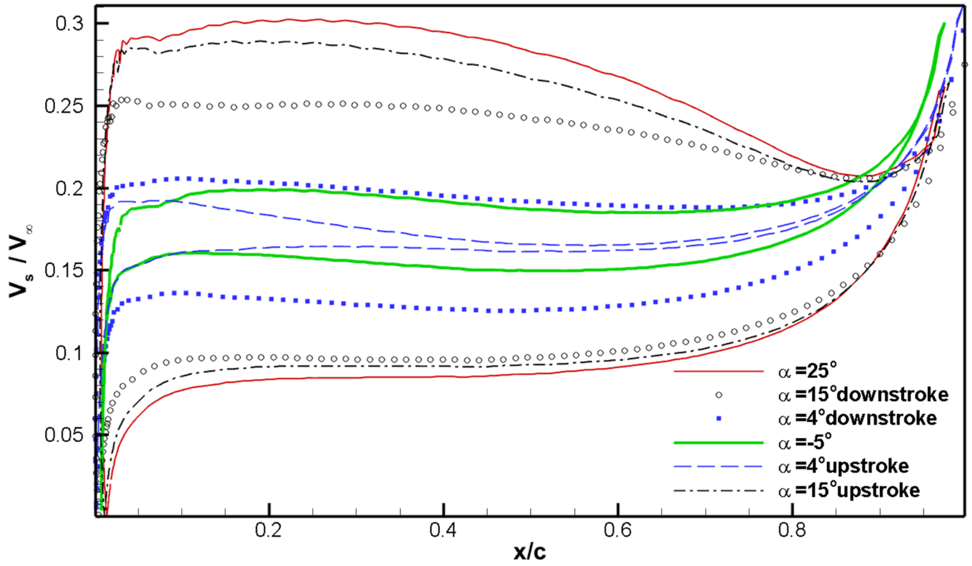

Fig. 12 The slip velocity distribution over the airfoil for Kn = 0.026, $k = 0.1$, $\alpha_m = 10°$ and $\alpha_A = 15°$

the airfoil, both numerical results are in good agreement with experimental results. However, in comparison with Gharali and Johnson (2013) the current lift and drag are closer to the experimental data at the down-stroke motion.

7 Results and Discussion

In this paper, the slip/jump boundary conditions of the OpenFOAM package are modified to handle the dynamic mesh related to the moving boundary on airfoil. In order to verify the accuracy of slip/jump boundary conditions under the pitching motion of the airfoil, the results of these boundary conditions at Kn = 0.001 are compared to the no-slip boundary conditions. This comparison for $k = 0.1$, $\alpha_m = 10°$ and $\alpha_A = 15°$ is displayed in Fig. 7. As can be observed, there is a good agreement between the lift and drag coefficient obtained by both the no-slip boundary condition and the slip boundary condition at Kn = 0.001. Therefore, the slip/jump boundary conditions have sufficient accuracy for simulating the pitching airfoil. In all simulations, the maximum Courant number is set to 0.1 with an initial time step of 1e−8. As shown in Amini et al. (2018), this value of maximum Courant number complies with the time step independence for results.

Mach number contours around the airfoil at different angles of attack during one period of airfoil pitching are shown in Fig. 8 for Kn = 0.026, $k = 0.1$, $\alpha_m = 10°$ and $\alpha_A = 15°$. In this case, the maximum and minimum values of α are 25° and −5°. In the first three contours of this figure, the airfoil rotates in the down-stroke direction and in the remaining contours it rotates in the upward direction. As can be observed, the contour of Mach number in $\alpha = 4°$ and 15° when the airfoil rotates in an upward direction differs from the contour in those values of α and a downward direction. This generates different values of lift and drag coefficient in up-stroke and down-stroke directions. Therefore, the lift and drag coefficients have different curves in up-stroke and down-stroke directions.

As shown in Fig. 8, a curvilinear shock is generated in front of the airfoil. The shape of shock and its curvature depend on the Mach number. At high Kn numbers, this shock is weakened and converted into some compression waves in front of the airfoil. At lower Kn numbers, freestream fluid flow has a higher density and consequently higher kinetic energy. As a result, the shock waves are strengthened and approach the leading edge of the airfoil.

The streamlines of fluid flow at different angles during one period of airfoil oscillation is presented in Fig. 9. It can be seen that there are no vortices and consequently no separation occurs in all angles of attack ranging from −5° to 25°. Similar results were observed by Shoja-Sani et al. (2014) in which a separation zone was observed at $M = 0.8$ while in supersonic flow, even at higher angles of attack up to 55°, the separation zone was not observed. This is associated with the higher total kinetic energy of in supersonic flow in comparison with subsonic flow.

In Fig. 10, the pressure coefficient distribution over the airfoil surface at different angles of attack in one pitching cycle for Kn = 0.026, $k = 0.1$, $\alpha_m = 10°$ and $\alpha_A = 15°$ is presented. As seen, the pressure coefficient changes with attack angle significantly. Moreover, the direction of rotation

Fig. 13 The lift and drag coefficients at various Kn number for $k = 0.1$, $\alpha_m = 10°$ and $\alpha_A = 15°$

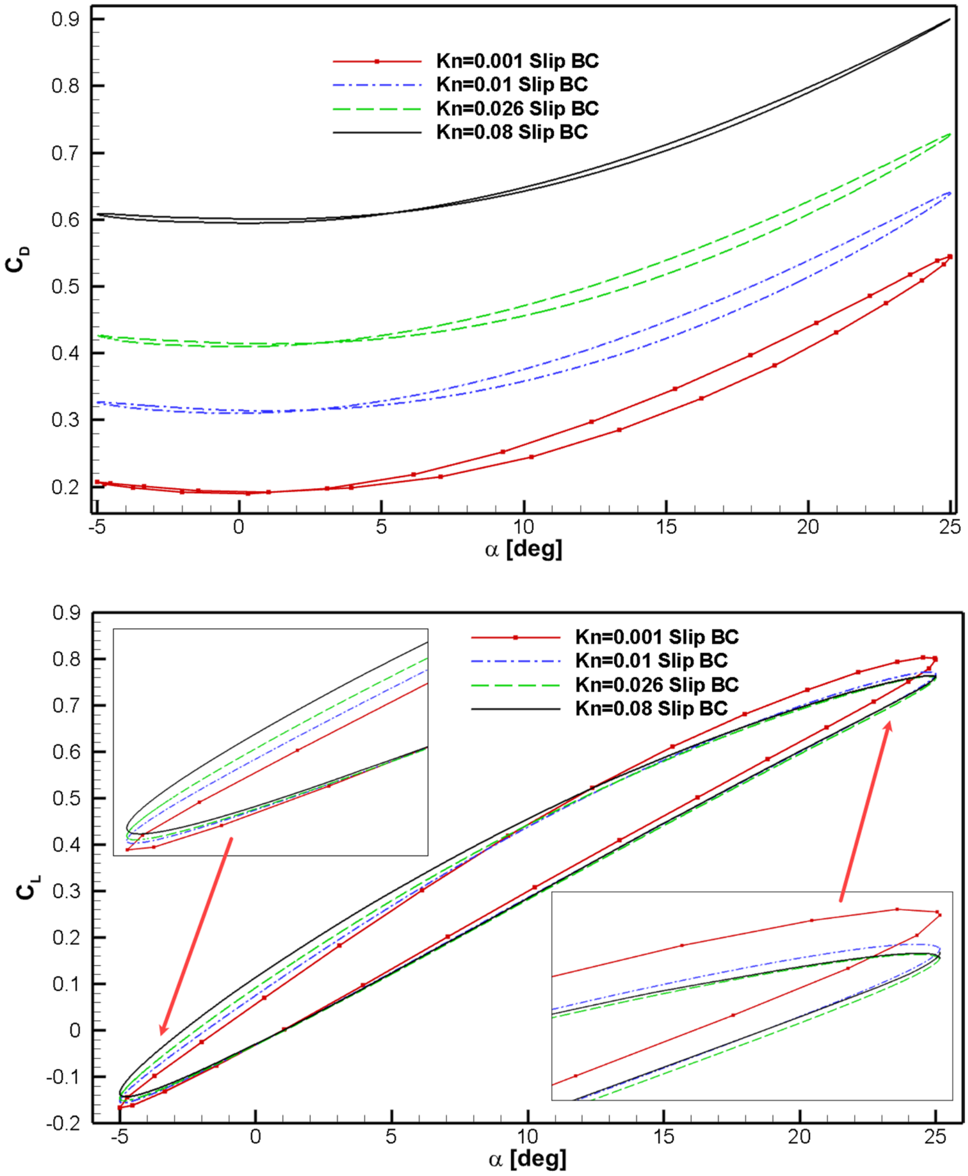

also has significant effect on the pressure coefficient. The effect of rotation direction at $\alpha = 4°$ is larger than its effect at $\alpha = 15°$. The difference between the lower and upper pressure coefficient has it maximum at $\alpha = 25°$. This difference is decreased by decreasing angles of attack from 25° to −5°. An angle of −5° is the minimum value of attack angle, and after that α is increased. By increasing α from −5° to 4°, the difference between the lower and upper pressure coefficient decreases and this difference has its minimum value at 4° up-stroke. Also, it can be seen that the difference of pressure coefficient in the front edge is larger than its value on the rear edge.

Figure 11 shows the temperature distribution over the airfoil surface at different angles of attack in one pitching cycle for $\mathrm{Kn} = 0.026$, $k = 0.1$, $\alpha_m = 10°$ and $\alpha_A = 15°$. As can be seen, the surface temperature at $\alpha = 25°$ has its maximum value and at $\alpha = 4°$ up-stroke has its minimum values. Surface temperatures are very different between the up-stroke and down-stroke directions at $\alpha = 15°$. However, their difference at $\alpha = 4°$ is negligible.

In Fig. 12, the slip velocity on the airfoil surface for $\mathrm{Kn} = 0.026$, $k = 0.1$, $\alpha_m = 10°$ and $\alpha_A = 15°$ is displayed. At $\alpha = 25°$ the slip velocity has its maximum value. By decreasing the angle of attack in down-stroke phase, the slip velocity decreases. This reduction is continued in the first portion of the up-stroke phase. The slip velocity reaches its minimum value at $\alpha = 4°$. After that the slip velocity increases. At $\alpha = 15°$ the slip velocity at lower surface of airfoil is approximately equal for both

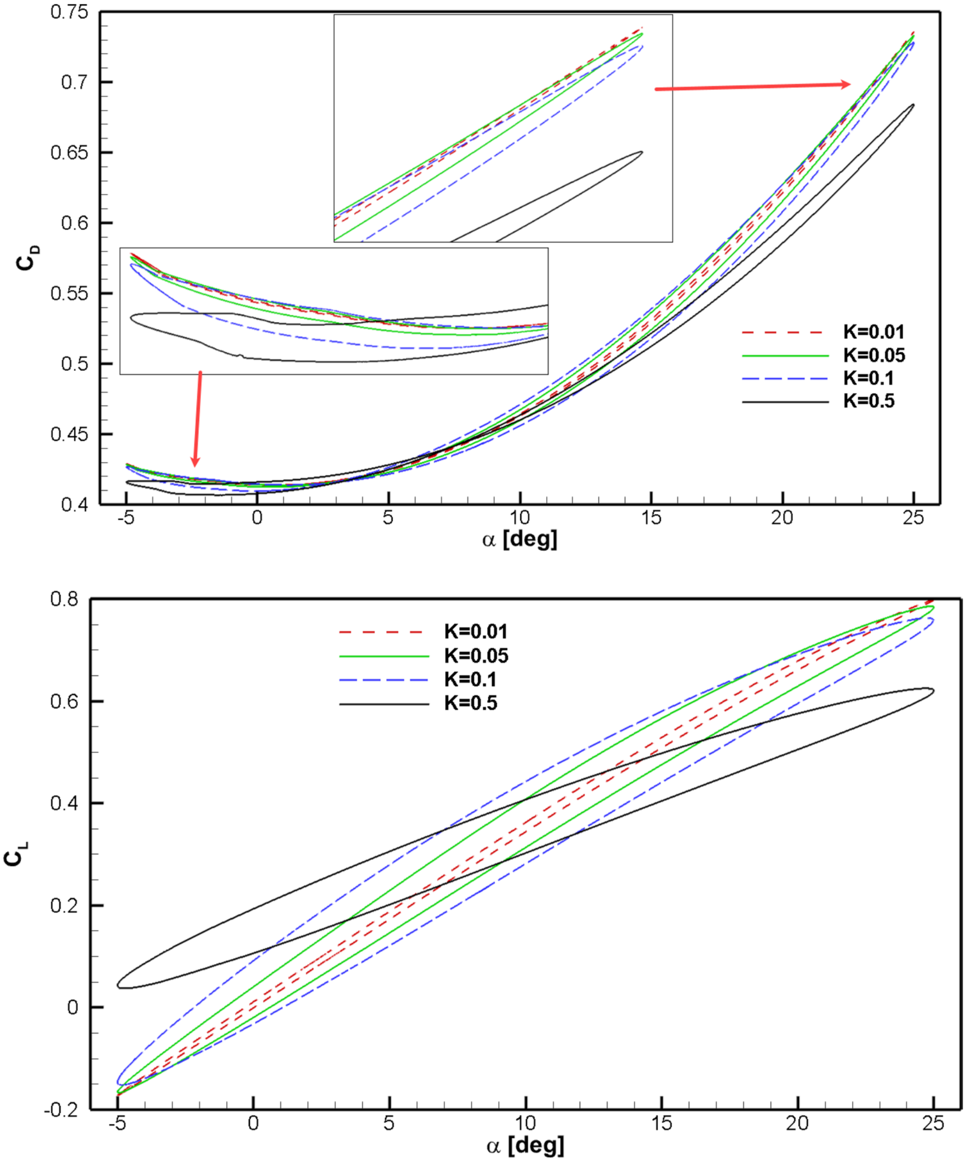

Fig. 14 The lift and drag coefficients at different values of reduced frequency for $\mathrm{Kn} = 0.026$, $\alpha_{\mathrm{m}} = 10°$ and $\alpha_{\mathrm{A}} = 15°$

down-stroke and up-stroke phases. However, at the upper surface of the airfoil, slip velocity in the up-stroke direction is greater than its value in the down-stroke direction. At $\alpha = 4°$, over the entire surface of the airfoil slip velocity in the down-stroke phase is greater than its value in the up-stroke phase.

Variations of the lift and drag coefficients with angle of attack at different values of Knudsen number for $k = 0.1$, $\alpha_{\mathrm{m}} = 10°$ and $\alpha_{\mathrm{A}} = 15°$ are shown in Fig. 13. By increasing the Knudsen number, the drag coefficient increases. Moreover, the path of the up-stroke and down-stroke of the drag coefficient are close to each other. At $\mathrm{Kn} = 0.08$, the up-stroke path approximately coincides with the down-stroke path. Dispute to the drag coefficient, the Kn number has not significant effect on the lift coefficient. However, its effects near maximum (25°) and minimum (−5°) angles are greater than its effect at other angles.

In Fig. 14 effects of reduced frequency on the lift and drag coefficients for $\mathrm{Kn} = 0.026$, $\alpha_{\mathrm{m}} = 10°$ and $\alpha_{\mathrm{A}} = 15°$ are shown. As it can be seen, reduced frequency smaller than $k = 0.1$ has a slight influence on the drag coefficient. However, $k = 0.5$ reduces the drag coefficient with respect to its values related to $k < 0.1$. Contrary to the drag coefficient, the reduced frequency has great influence on the lift coefficient. As can be seen, by increasing the reduced frequency, the lift loop becomes thicker and rotates in the clockwise

Fig. 15 The lift and drag coefficients at different values of the mean angle for Kn = 0.026, k = 0.1 and $\alpha_A = 15°$

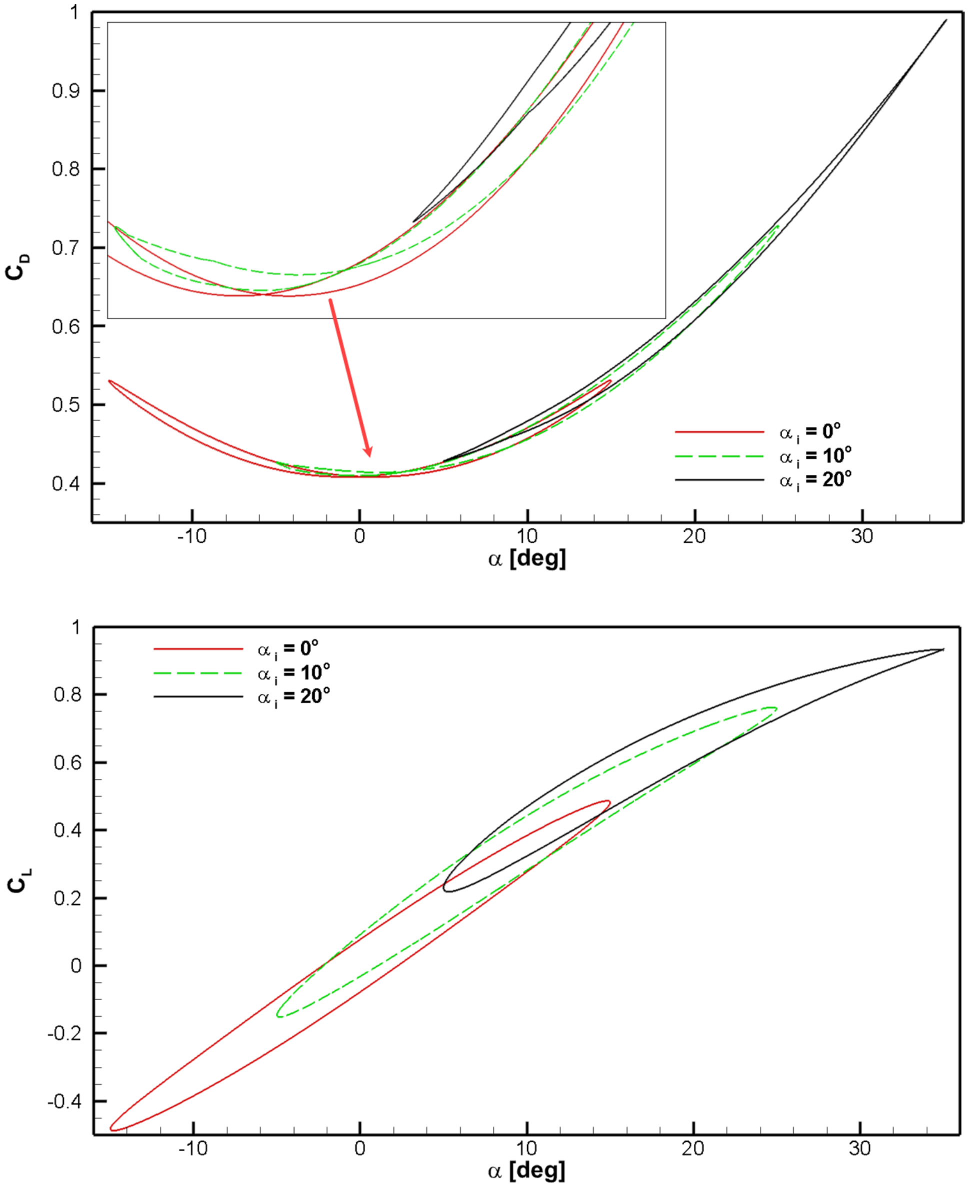

direction around the mean angle $\alpha_m = 10°$. During the pitching motion, the dynamic cambering effect leads to a larger maximum value of lift coefficient. Dynamic cambering is caused by fluid flowing on the suction surface that experiences a greater curvature when the airfoil rotates rapidly, resulting in a larger lift. This phenomenon occurs only in an attached boundary condition. Since in the high Mach number rarefied gas flow boundary layer separation does not happen, the dynamic cambering improves the lift coefficient.

The changes of the lift and drag coefficients for different values of the mean angle (α_m) in fixed values of Kn = 0.026, $k = 0.1$ and $\alpha_A = 15°$ are shown in Fig. 15. By increasing the mean angle, the lift values at the maximum and minimum angle of attack are increased and decreased, respectively. Moreover, the increase in the mean angle of attack shifts the lift loop considerably to the higher values.

The variations of the lift and drag coefficients at Kn = 0.026, $k = 0.1$ and $\alpha_m = 10°$and different values of pitching amplitude are presented in Fig. 16. By increasing the pitching amplitude, the drag coefficient loop enlarges and become thicker. For $\alpha_A = 5°$, $\alpha_A = 10°$ and $\alpha_A = 15°$ the maximum values of drag coefficient are 0.54, 0.62 and 0.73, respectively.

Fig. 16 The lift and drag coefficients at different values of pitching amplitude for Kn = 0.026, $k = 0.1$ and $\alpha_m = 10°$

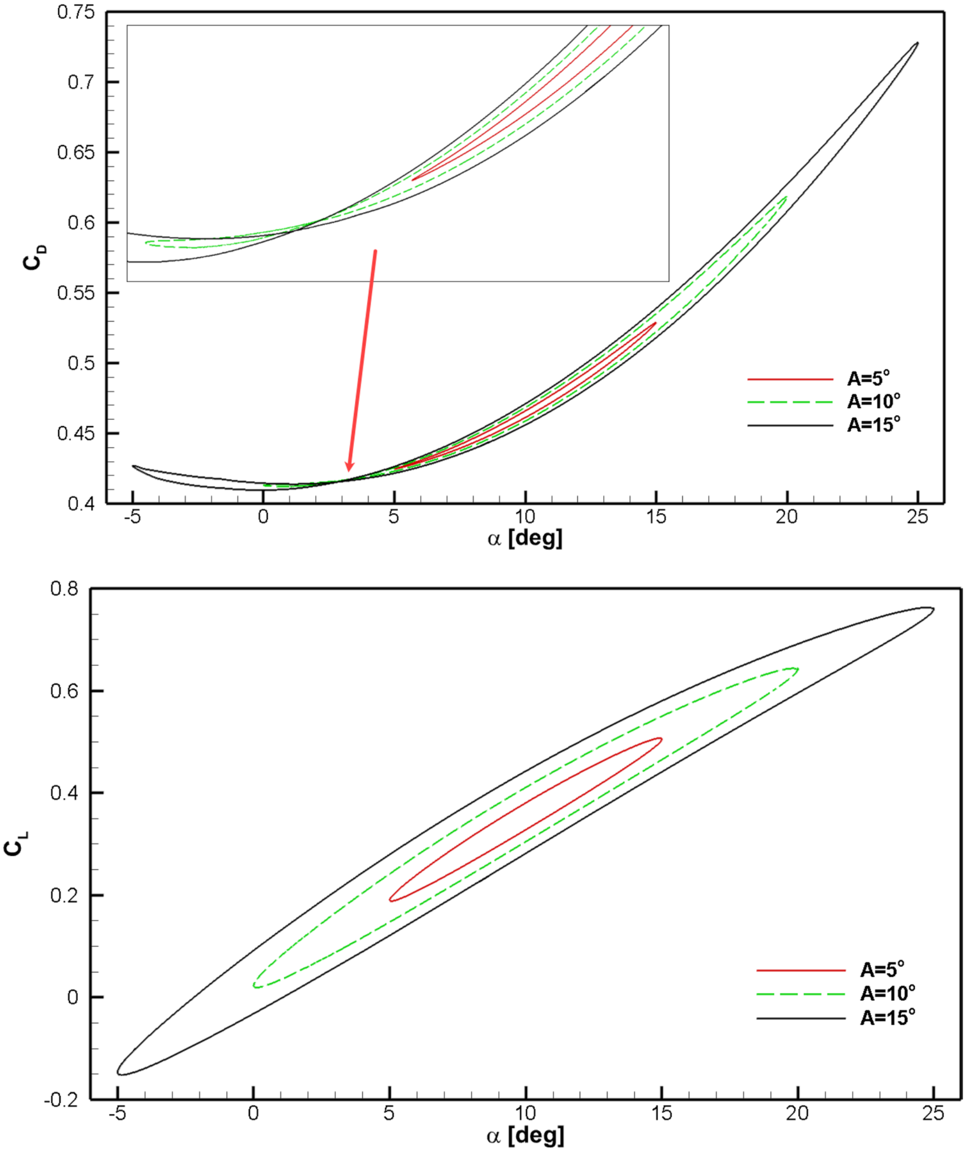

8 Conclusions

In this study, the effects of pitching amplitude, mean angle of attack and Knudsen number on the lift and drag coefficients of the NACA 0012 airfoil were numerically investigated. The Knudsen number was chosen in the slip flow regime. Therefore, the N–S equations with Maxwell slip and Smoluchowski jump boundary conditions were solved as governing equations of flow. It was concluded that both the angle of attack and rotation direction substantially affect the pressure coefficient, slip velocity and wall temperature. Moreover, The Kn number has no significant effect on the lift coefficient but changes the drag coefficient significantly. It was shown that the reduced frequency changes the lift coefficient considerably, but its effect on the drag coefficient is negligible.

Data Availability The output data that support the findings of this study are available from the corresponding author upon reasonable request.

Declarations

Conflict of interest The author declares that he has no known competing financial interests or personal relationships that could have appeared to influence the work reported in this paper.

References

Allegre J, Raffin M, Gottesdiener L (1986) Slip effects on supersonic flowfields around NACA 0012 airfoils. In: International symposium on rarefied gas dynamics, 15th, Grado, Italy, pp 54–557

Allegre J, Raffin M, Lengrand J (1987) Experimental flowfields around NACA 0012 airfoils located in subsonic and supersonic rarefied air streams. In: Bristeau MO, Glowinski R, Periaux J, Viviand H (eds) Numerical simulation of compressible Navier–Stokes flows. Springer, Berlin

Amini Y, Emdad H, Akramian K, Bordbar F (2012) Investigation of the common nose cone shapes in different gas mixtures in high Knudsen numbers. Sci Iran 19:1511–1518

Amini Y, Liravi M, Izadpanah E (2018) The effects of Gurney flap on the aerodynamic performance of NACA 0012 airfoil in the rarefied gas flow. Comput Fluids 170:93–105

Amiralaei M, Alighanbari H, Hashemi S (2010) An investigation into the effects of unsteady parameters on the aerodynamics of a low Reynolds number pitching airfoil. J Fluids Struct 26:979–993

Bird GA (1976) Molecular gas dynamics. NASA STI/Recon Technical Report A, 76

Chambré PL, Schaaf SA (1961) Flow of rarefied gases. Princeton University Press, Princeton

Fan J, Boyd ID, Cai C-P, Hennighausen K, Candler GV (2001) Computation of rarefied gas flows around a NACA 0012 airfoil. AIAA J 39:618–625

Favier D, Agnes A, Barbi C, Maresca C (1988) Combined translation/pitch motion-a new airfoil dynamic stall simulation. J Aircraft 25:805–814

Gad-El-Hak M (1999) The fluid mechanics of microdevices-the Freeman scholar lecture. Trans Am Soc Mech Eng J Fluids Eng 121:5–33

Gharali K, Johnson DA (2013) Dynamic stall simulation of a pitching airfoil under unsteady freestream velocity. J Fluids Struct 42:228–244

Greenshields CJ, Weller HG, Gasparini L, Reese JM (2010) Implementation of semi-discrete, non-staggered central schemes in a colocated, polyhedral, finite volume framework, for high-speed viscous flows. Int J Numer Methods Fluids 63:1–21

Ho C-M, Tai Y-C (1998) Micro-electro-mechanical-systems (MEMS) and fluid flows. Annu Rev Fluid Mech 30:579–612

Karniadakis G, Beskok A, Aluru N (2006) Microflows and nanoflows: fundamentals and simulation. Springer, Berlin

Ko S, Mccroskey W (1997) Computations of unsteady separating flows over an oscillating airfoil. AIAA J 35:1235–1238

Kurganov A, Tadmor E (2000) New high-resolution central schemes for nonlinear conservation laws and convection–diffusion equations. J Comput Phys 160:241–282

Kurganov A, Noelle S, Petrova G (2001) Semidiscrete central-upwind schemes for hyperbolic conservation laws and Hamilton–Jacobi equations. SIAM J Sci Comput 23:707–740

Le NT, Shoja-Sani A, Roohi E (2015) Rarefied gas flow simulations of NACA 0012 airfoil and sharp 25–55-deg biconic subject to high order nonequilibrium boundary conditions in CFD. Aerosp Sci Technol 41:274–288

Lee T, Gerontakos P (2004) Investigation of flow over an oscillating airfoil. J Fluid Mech 512:313–341

Leishman J (1990) Dynamic stall experiments on the NACA 23012 aerofoil. Exp Fluids 9:49–58

Lilley CR, Sader JE (2008) Velocity profile in the Knudsen layer according to the Boltzmann equation. Proc R Soc Lond A Math Phys Eng Sci 464:2015–2035

Martin J, Empey R, Mccroskey W, Caradonna F (1974) An experimental analysis of dynamic stall on an oscillating airfoil. J Am Helicopter Soc 19:26–32

Shoja-Sani A, Roohi E, Kahrom M, Stefanov S (2014) Investigation of aerodynamic characteristics of rarefied flow around NACA 0012 airfoil using DSMC and NS solvers. Eur J Mech B Fluids 48:59–74

Wang S, Ingham DB, Ma L, Pourkashanian M, Tao Z (2010) Numerical investigations on dynamic stall of low Reynolds number flow around oscillating airfoils. Comput Fluids 39:1529–1541

Wernert P, Geissler W, Raffel M, Kompenhans J (1996) Experimental and numerical investigations of dynamic stall on a pitching airfoil. AIAA J 34:982–989

Zhang W-M, Meng G, Wei X (2012) A review on slip models for gas microflows. Microfluid Nanofluid 13:845–882